Hybrid-order topology in unconventional magnets of Eu-based Zintl compounds with surface-dependent quantum geometry

Yufei Zhao,[1] Yiyang Jiang,[1] Hyeonhu Bae,[1] Kamal Das,[1] Yongkang Li,[1] Chao-Xing Liu,[2] and Binghai Yan[1,*]

[1]*Department of Condensed Matter Physics, Weizmann Institute of Science, Rehovot 7610001, Israel*

[2]*Department of Physics, the Pennsylvania State University, University Park, Pennsylvania 16802, USA*

(Received 1 March 2024; revised 1 September 2024; accepted 8 October 2024; published 5 November 2024)

The exploration of magnetic topological insulators is instrumental in exploring axion electrodynamics and intriguing transport phenomena, such as the quantum anomalous Hall effect. Here, we report that a family of magnetic compounds $Eu_{2n+1}In_2(As,Sb)_{2n+2}$ ($n = 0, 1, 2$) exhibit both gapless Dirac surface states and chiral hinge modes. Such a hybrid-order topology hatches surface-dependent quantum geometry. By mapping the responses into real space, we demonstrate the existence of chiral hinge modes along the c direction, which originate from the half-quantized anomalous Hall effect on two gapped ac/bc facets due to Berry curvature, while the unpinned Dirac surface states on the gapless ab facet generate an intrinsic nonlinear anomalous Hall effect due to the quantum metric. When $Eu_3In_2As_4$ is polarized to the ferromagnetic phase by an external magnetic field, it becomes an ideal Weyl semimetal with a single pair of type-I Weyl points and no extra Fermi pocket. Our work predicts rich topological states sensitive to magnetic structures, quantum geometry-induced transport, and topological superconductivity if proximitized with a superconductor.

DOI: 10.1103/PhysRevB.110.205111

I. INTRODUCTION

Topological quantum states of matter are usually characterized by unique boundary states following the bulk-boundary correspondence [1–3]. To be specific, a topological insulator (TI) exhibits two-dimensional (2D) Dirac-type surface states [4,5] and a higher-order TI shows 1D hinge states [6–9]. Unlike nonmagnetic topological crystalline insulators (TCI) [6,7,10–12], surface/hinge states in a magnetic TCI are intimately related to magnetic structures [8]. Applying a magnetic field to flip or rotate spin moments is equivalent to reversing the mass signs of the gapped surface, thus switching the chirality of hinge states and the mapped 2D Chern number [8,13–17]. Identifying the nature of topological invariants under a combined magnetic crystalline symmetry by the translation (τ) or n-fold rotation (C_n) with time-reversal ($\mathcal{T}$) is evidently a central issue [18–22]. For instance, $MnBi_2Te_4$ is a $\tau\mathcal{T}$ protected antiferromagnetic (AFM) TI with gapless Dirac surface parallel to τ [23–25], namely, a first-order topology depicted in Fig. 1(a). A hybrid-order topological phase [e.g., Figs. 1(b) and 1(c)], which exhibits both topological surface states and hinge states, is rare among intrinsic magnetic materials [14].

Furthermore, a magnetic TCI with $\tau\mathcal{T}$ or $C_n\mathcal{T}$ symmetry can generate axion electrodynamics, described by the so-called quantized θ term [26], $S_\theta = \int dtd^3x \frac{\theta e^2}{4\pi^2\hbar c}\boldsymbol{E}\cdot\boldsymbol{B}$, where $\boldsymbol{E}$ and $\boldsymbol{B}$ are external electric and magnetic fields, and θ is the axion field defined in a 3D system [23,24,27–30]. Axion insulators manifest a half-quantized anomalous Hall conductance (AHC) of $\pm\frac{e^2}{2h}$ on the gapped surface [3,31,32], which comes from Berry curvature, i.e., the imaginary part of the quantum geometry tensor [33,34]. When two adjacent gapped surfaces hold opposite masses, the surface quantum anomalous Hall effect (QAHE) is carried by the 1D chiral hinge mode [35]. On the other side, the real part of the quantum geometry—quantum metric—was recently discovered to generate nonlinear anomalous Hall effect (NLAHE) in magnetic conductors [36–40]. We are inspired to ask whether metallic surface states can generate a surface NLAHE due to the quantum metric in a magnetic TCI.

Recently, Eu-based Zintl compounds $Eu_{2n+1}In_2(As,Sb)_{2n+2}$ ($n = 0, 1, 2$) emerged with unusual magnetic structures revealed by neutron diffraction, resonant elastic x-ray scattering, muon spin rotation, or magnetotransport [41–52]. These materials can be magnetic TCI candidates due to the interplay of AFM order and strong spin-orbit coupling (SOC). In $EuIn_2As_2$, a pure helix order formed at 17.5 K evolves to a "broken helix order" below 16 K [Fig. 1(d)] [42–46], although an earlier theory study assumed a collinear AFM order [15]. In $Eu_3In_2As_4$, an AFM order was confirmed below $5 \sim 6.5$ K in experiments [51,52]. In $Eu_5In_2As_6$, a collinear AFM order formed at 14 K [Fig. 1(f)] evolves to a complex coplanar order below 7 K accompanied with the anisotropic susceptibility [47–50]. Their magnetic structures of three compounds exhibit $C_2\mathcal{T}$ symmetry but break $\tau\mathcal{T}$ and $\mathcal{PT}$, different from the conventional AFM phase (e.g., $MnBi_2Te_4$) but similar to "altermagnets," a collinear AFM order studied recently [53–57]. Additionally, $Eu_3In_2As_4$ was recently grown from InAs nanowires in a mutual-exchange method [51] and inherits the ideal proximity with a superconductor [58]. Thus, this system will serve as a potential platform to study topological superconductivity due to the interplay between chiral hinge states/Dirac surface states and the s-wave superconductivity.

*Contact author: binghai.yan@weizmann.ac.il

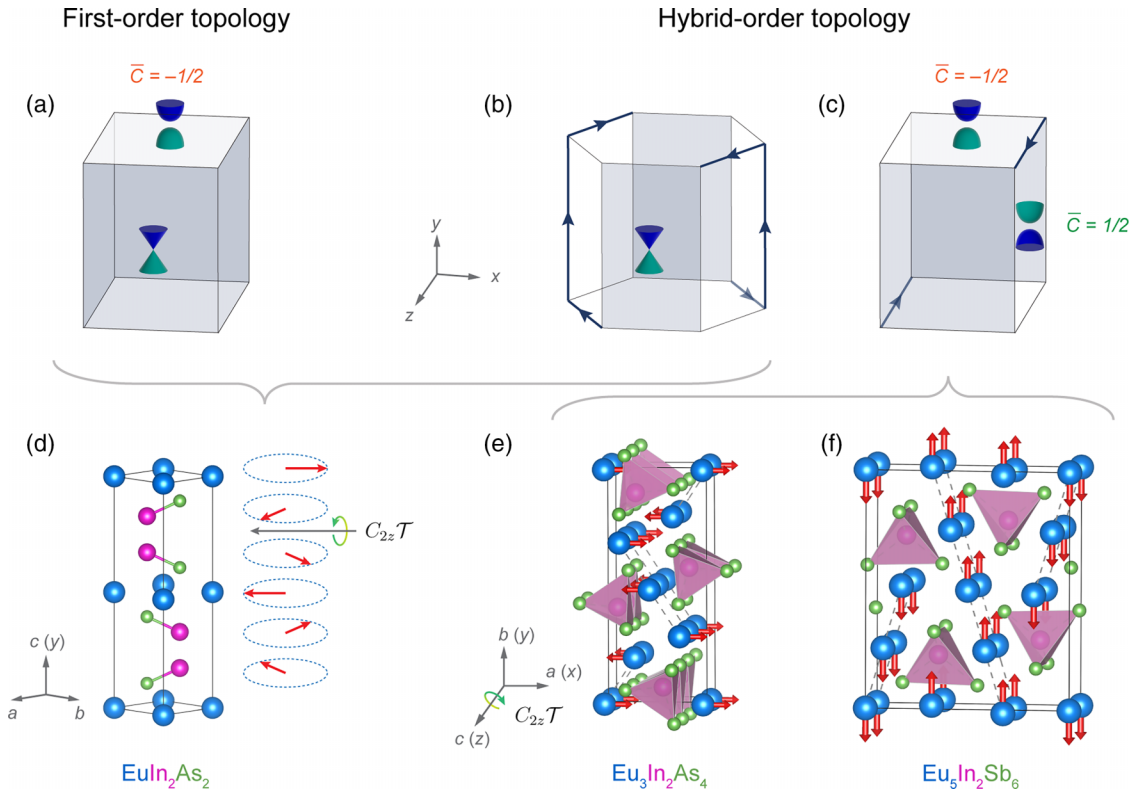

FIG. 1. Symmetry protected boundary states, crystal and magnetic structures. (a) The first-order topology with gapless surfaces (dark) protected by $\tau_y\mathcal{T}$ symmetry, exemplified by $MnBi_2Te_4$. (b), (c) The hybrid-order topology with unpinned Dirac surfaces (dark) and chiral hinge states (thick lines) under $C_{2z}\mathcal{T}$ symmetry, exemplified by $Eu_{2n+1}In_2(As,Sb)_{2n+2}$. (b) and (c) show two kinds of sample geometry. (d) $EuIn_2As_2$ (space group: $P6_3/mmc$): Broken helix spin order (in the *ab* plane) below 16 K [44–46]. Six layers of Eu atoms (dashed ellipses) form a period. (e) $Eu_3In_2As_4$ (*Pnnm*): AFM order predicted by calculations. The thin dashed lines mark a set of sublattices. (f) $Eu_5In_2Sb_6$ (*Pbam*): Collinear magnetic order between 7 and 14 K [49,50]. Below 7 K, the spin order becomes coplanar but $C_{2z}\mathcal{T}$ symmetry still survives. For $Eu_3In_2As_4$ and $Eu_5In_2Sb_6$, the $C_{2z}\mathcal{T}$ axis passes through the cell center.

In this work, we predict that $Eu_{2n+1}In_2(As,Sb)_{2n+2}$ compounds possess hybrid-order topology characterized by the coexistence of chiral hinge modes and unpinned Dirac surface states protected by a $C_2\mathcal{T}$-related topological invariant [19–22]. Taking $Eu_3In_2As_4$ for an example, we demonstrate the axion insulator state with a surface QAHE. On the gapless surface, we find the NLAHE due to the quantum metric from Dirac states. In addition, the AFM bulk can exhibit the anomalous Hall effect despite vanishing net magnetization, because the magnetic lattice violates $\tau\mathcal{T}$ and $\mathcal{P}\mathcal{T}$. If the magnetic order turns ferromagnetic (FM) by applying a magnetic field, $Eu_3In_2As_4$ exhibits an ideal Weyl semimetal phase. We further derive a topological phase diagram based on a material-specific effective model to reveal possible topological states for these compounds in different magnetic orders. Finally, we discuss possible unique Majorana modes when the material is in proximity to an ordinary superconductor.

II. RESULTS

A. Magnetic order and bulk band structure

We first focus on $Eu_3In_2As_4$ to demonstrate the hybrid-order topology and resultant properties. As illustrated in Fig. 1(e), the Zintl compound $Eu_3In_2As_4$ crystallizes in an orthorhombic lattice with the inversion symmetric space group *Pnnm*, including a twofold rotation C_{2z}, and nonsymmorphic symmetries $\{C_{2x,2y}|\tau\}$, where τ is the translation of one-half of a body diagonal $(\frac{a}{2}, \frac{b}{2}, \frac{c}{2})$. All atoms are located at $z = 0$ and $z = 0.5$ planes, and one In atom and four As atoms form a tetrahedron. The tetrahedrons ($[In_2As_4]^{6-}$) constitute a 1D chain by sharing their corners along the c axis, between which the divalent Eu^{2+} cations ($\mathbf{S} = \frac{7}{2}$) are dispersed. Three Eu atoms (linked by the dashed line) with the two nearest neighboring tetrahedrons form a sublattice. Within one unit cell, two sublattices are related by $\{C_{2x,2y}|\tau\}$ operations.

The exact spin structure has thus far not been resolved in experiments, so we carry out the calculations to examine the magnetic ground state of $Eu_3In_2As_4$. Inspired by the collinear spin order of the sister compound $Eu_5In_2As_6$ [49,50], we investigated several collinear magnetic structures (Table III in the Supplemental Material [59]). We found an AFM phase with the easy axis in the *ab* plane [Fig. 1(e)] is energetically favored, consistent with recent magnetometry measurements [51,52]. The Eu^{2+} cations exhibit FM coupling along the c axis while two sublattices are AFM coupled. The in-*ab*-plane magnetic structure preserves $C_{2z}\mathcal{T}$ symmetry.

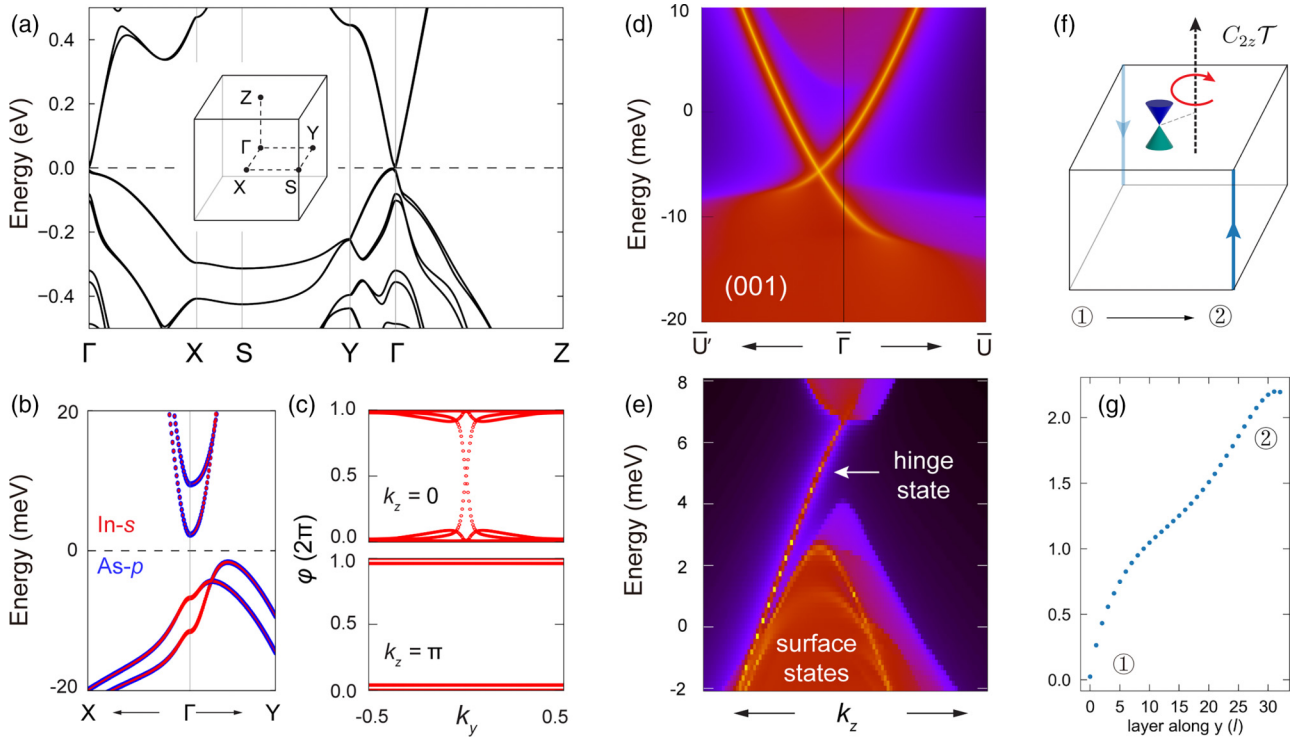

FIG. 2. Bulk-surface-hinge correspondence in $Eu_3In_2As_4$. (a) Bulk band structure. (b) Inverted band gap with orbital weights. (c) The 1D k_x-integrated Wilson bands on the $k_z = 0/\pi$ planes. (d) (001) surface states. $\bar{U}$ is not a high-symmetry point. (e) The hinge state flowing along the c axis, calculated in a finite 34.5 unit cell along the b axis ($\hat{y}$) and semi-infinite along a axis ($\hat{x}$). (f) Schematic illustration of the unpinned Dirac point under $C_{2z}\mathcal{T}$. Hinges 1/2 are adjacent by the bc facet and ac facet. (g) The intensity of the in-gap states [pointed in (e)] projected onto each layer (unit cell), showing a localization behavior at hinge 2. No. 0 and No. 35 represent two hinges.

The nonmagnetic phase gives a trivial semiconducting band structure while magnetic orders lead to nontrivial topology. The band structure of $Eu_3In_2As_4$ with an AFMa order (easy axis along a) is shown in Fig. 2(a). Localized Eu-4f orbitals appear below the Fermi energy between -2.5 eV and -1.5 eV. Without SOC, a trivial bandgap of 52 meV is found at the Γ point and spin splitting appears along $\Gamma - S$ (see Fig. S9 in the Supplemental Material [59]). The inclusion of SOC induces an inverted gap of nearly 10 meV at Γ with band inversion and an indirect global gap of 5 meV [Fig. 2(b)], which is larger than the energy scale of magnetic order temperature ($T_N \sim 5$ K) or the induced superconductivity gap. The spin double-degeneracy is lifted along $\Gamma - X$, $\Gamma - Y$, and $\Gamma - Z$, similar to an altermanget, but remains along $X - S - Y$ because of antiunitary operators $\{C_{2x}|\tau\}\mathcal{T}$ and $\{M_x|\tau\}\mathcal{T}$. Details of symmetry analysis can be found in Sec. SIII in the Supplemental Material [59].

B. Surface and hinge states

The antiunitary symmetry $C_{2z}\mathcal{T}$ helps understand the bulk-surface-hinge correspondence. Let us begin with a $\mathcal{T}$-preserved $\mathbb{Z}_2$ TI where all surfaces present Dirac surface states. For an orthorhombic crystal [Fig. 1(c)], magnetism opens a surface gap on bc and ac facets, i.e., introduces a mass term in the Dirac equation. Because they transform to each other by $C_{2z}\mathcal{T}$, two bc facets (also two ac facets) exhibit opposite masses. For four hinges between ac and bc facets along the c direction, we can always find two diagonal hinges at the domain boundary between surfaces with opposite signs of mass, leading to chiral hinge modes inside the surface gap. $C_{2z}\mathcal{T}$ symmetry is preserved on the ab plane and leads to crystalline symmetry-protected unpinned Dirac surface states. The surface Dirac cone can only be pushed away from time-reversal-invariant momenta (e.g., $\bar{\Gamma}$) rather than gapped out. Two chiral hinge states terminate at gapless (001) surfaces while the equilibrium current persists, different from an ordinary TI or TCI that shows only surface or hinge states. Consequently, three surface Chern numbers ($\overline{\mathbb{C}} = \pm\frac{1}{2}, 0$) can be realized on different surfaces, offering a road for designing the direction-selective QAHE and quantized circular dichroism effect [60].

Such a magnetic TCI is equivalent to a 3D strong Stiefel-Whitney insulator with vanishing Berry curvature due to $C_{2z}\mathcal{T}$ symmetry [20,21,61,62]. We can define a $\mathbb{Z}_2$-type topological invariant $\Delta_{3D} = w_2(\pi) - w_2(0)$, where $w_2(k_z)$ is the second Stiefel-Whitney number defined on a 2D plane. The first Stiefel-Whitney number w_1 is equivalent to the quantized Berry phase and thus $w_1 = 0$ in our case. A nontrivial w_2 characterizes a double band inversion, which is well defined only when $w_1 = 0$. We can calculate w_2 by tracing the Wilson loop spectra φ, where w_2 is the number of crossings at $\varphi = \pi$ mod 2. Figure 2(c) indicates the AFMa phase as a 3D strong Stiefel-Whitney insulator ($\Delta_{3D} = 1$) with $w_2(0) = 1$ and $w_2(\pi) = 0$. The Stiefel-Whitney insulator can exhibit an odd number of surface Dirac cones [19,21].

We perform the Green's function calculations using Wannier functions extracted from DFT calculations to verify

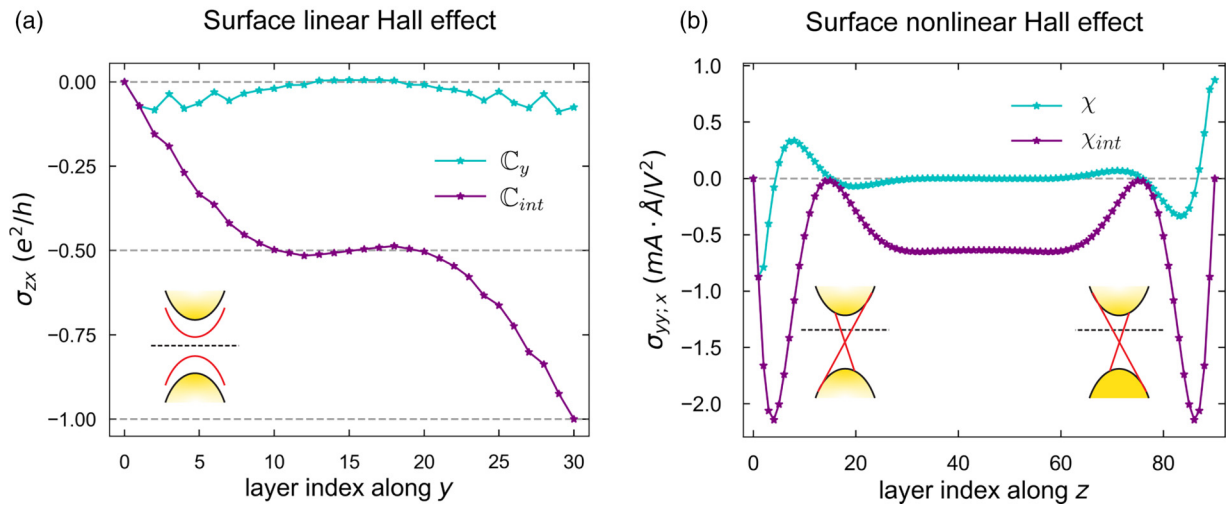

FIG. 3. Surface anomalous Hall effect. (a) Local Chern number and integrated Hall conductance as a function of layers in a 29.5 unit cell slab. (b) Intrinsic second-order Hall conductivity from the quantum metric dipole in a 90 unit cell slab. The Fermi level lies in the surface gap in (a) and cuts through the surface Dirac cone in (b).

the surface and hinge states. A single gapless Dirac cone exists on the (001) surface, shown in Fig. 2(d). Because there is no additional symmetry to constrain the Dirac point besides $C_{2z}\mathcal{T}$, the Dirac point is unpinned from $\bar{\Gamma}$ or any high-symmetry line. The Dirac point positions can be continuously shifted by synchronously rotating or slightly titling the magnetic moments on the *ab* plane (Fig. S5 in the Supplemental Material [59]), for which $C_{2z}\mathcal{T}$ is maintained. In this case, the in-plane magnetic moments act as a vector potential perturbation that keeps the gapless nature of the surface Dirac cone.

The hinge modes of two adjacent side facets are analyzed by building a half-infinite slab model, containing 34 unit cells plus half a unit cell (34.5) along the *b* axis, which respects $C_{2z}\mathcal{T}$ and is thick enough to suppress interfacet and interhinge interactions. The obtained spectrum includes the states from bulk, one (100) surface, two (010) surfaces, and two hinges. In Fig. 2(e), an up-moving in-gap state clearly emerges as we expect. By projecting it into each layer, we find that the spectral weight is mainly distributed at hinge ② [Fig. 2(g)], confirming it as a hinge mode in the real space. These exotic boundary states attract us to next consider what kind of transport signals or physical quantity they carry on the surface.

C. Surface quantum geometry

To resolve a local response in real space, we can introduce the non-Abelian quantum geometric tensor in terms of two band (n, m), and depose it as [63]

$$\mathcal{Q}^{ij}_{nm} \equiv \mathcal{A}^{i}_{nm}\mathcal{A}^{j}_{mn} = g^{ij}_{nm} - \frac{i}{2}\Omega^{ij}_{nm}, \tag{1}$$

where $\mathcal{A}^{i}_{nm} = i\langle n|\partial_{k_i}|m\rangle$ is the Berry connection, and g^{ij}_{nm} and $\Omega^{ij}_{vv'}$ are the quantum metric and Berry curvature. Then the local AHC in a slab is identified by the layer-resolved Chern number $\sigma^{ij}_{\text{slab}}(l) = \frac{e^2}{h}\mathbb{C}(l)$ [32],

$$\sigma^{ij}_{\text{slab}}(l) = \frac{e^2}{\pi h}\text{Im}\sum_{n=1}^{N_c}\sum_{m=N_c+1}^{\infty}\int_{\boldsymbol{k}}\frac{\langle n|\hat{P}_l\partial_{k_i}\mathcal{H}|m\rangle\langle m|\partial_{k_j}\mathcal{H}|n\rangle}{(\varepsilon_n-\varepsilon_m)^2}, \tag{2}$$

where N_c is the number of occupied bands, and $\hat{P}_l = |l\rangle\langle l|$ is the projector onto lth layer.

By constructing a slab along the y direction, $\mathbb{C}_y(l)$ and $\mathbb{C}_{\text{int}}(l) = \sum_{l'=0}^{l}\mathbb{C}_y(l')$ in Fig. 3(a) show a saturation behavior of the half-quantized surface AHC. Such a local signal is known to be the direct evidence of the axion insulator [32]. The first ten layers are enough to stabilize $\mathbb{C}_{\text{int}}$ at 0.4976 (corresponds to the penetration length of the hinge state), while the internal layers from No. 10 to No. 20 (bulk) tame the oscillation and do not contribute to σ^{zx} of the entire slab. Since the spin moments of the top and bottom layers hold the same direction, the half-quantized surface AHC from the first and last ten layers together gives rise to a $\mathbb{C} = -1$ Chern insulator.

Besides the surface AHC, it is worth noting that $C_{2z}\mathcal{T}$ does not exclude all the bulk Hall tensors. When the system is doped to be a conductor, a finite AHC $\sigma^{zx}_{\text{bulk}}$ will also emerge despite the compensated magnetization (Fig. S10 in the Supplemental Material [59]), offering a signature of unusual antiferromagnet or altermagnet.

On the $C_{2z}\mathcal{T}$-preserved *ab* facet, the linear AHC σ^{xy} vanishes but the second-order Hall conductivity is permitted ($\sigma^{ij;k} = \mathcal{J}^k/E^iE^j$) [40]. In a similar vein, the layer-resolved second-order Hall conductivity can be given by

$$\sigma^{ii;j}_{\text{slab}}(l) = \frac{e^3}{\hbar}\text{Re}\sum_{n,m\neq n}^{\infty}\int_{\boldsymbol{k}}\frac{2\langle n|\hat{P}_l\partial_{k_j}\mathcal{H}|n\rangle\langle n|\partial_{k_i}\mathcal{H}|m\rangle\langle m|\partial_{k_i}\mathcal{H}|n\rangle - \langle n|\hat{P}_l\partial_{k_i}\mathcal{H}|n\rangle\langle n|\partial_{k_i}\mathcal{H}|m\rangle\langle m|\partial_{k_j}\mathcal{H}|n\rangle}{(\varepsilon_n-\varepsilon_m)^3}\frac{\partial f_n}{\partial\varepsilon_n}. \tag{3}$$

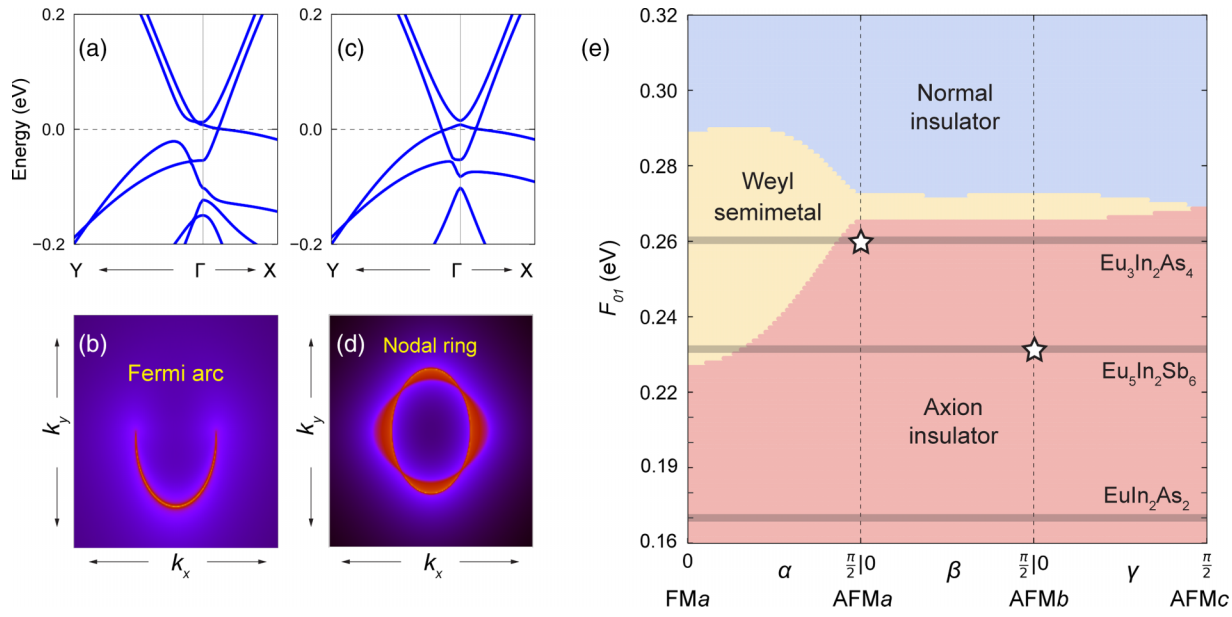

FIG. 4. Multiple magnetic topological phases in Zintl compounds. (a), (c) Band structure near the Γ point of the FMa and FMc phases. (b), (d) Projected (001) Fermi surface. The Fermi arc connects two Weyl points in (b). Symmetry M_z protects a Weyl nodal ring in (c). (e) Topological phase diagram in terms of SOC strength F_{01} and magnetic orders. Pentagrams along the gray line represent the ground states in Fig. 2(a) and Fig. S11 in the Supplemental Material.

Equation (3) includes the Fermi surface contribution from the scattering time-independent quantum metric dipole (χ^{QMD}). In Fig. 3(b), a localized intrinsic NLAHE is found in a slab stacked along the c direction. Due to the inversion symmetry, the total second-order conductivity [$\chi_{\mathrm{int}}(l=90)$] is zero and the Dirac cone from the top and bottom surfaces are oppositely titled. Since $C_{2z}\mathcal{T}$ does not restrict the shape of the Dirac cone, an in-plane nonlinear response $\sigma^{yy;x}$ will appear on the surface. Breaking inversion with different chemical potentials for the top and bottom surface states is expected to induce a net NLAHE in the thin film, which can be probed in transport experiments. In addition, both the surface AHE and surface NLAHE discussed above can also be measured by the nonlocal transport, for example, by using a device configuration proposed in Ref. [64].

D. Weyl semimetal phase

When all the spin moments align along the a axis under an external field (FMa, $\mathbf{m} \parallel a$), we find two type-I Weyl points with opposite chiralities along $\Gamma - X$ connected by inversion symmetry in Figs. 4(a) and 4(b). In the projected (001) Fermi surface, two Weyl nodes separated 0.074 Å^{-1} along k_x are connected by a surface Fermi arc. In the FMb phase (Fig. S7 in the Supplemental Material [59]), the Weyl nodes are shifted to locate along the $\Gamma - Y$ direction. Thus, the FM$a/b$ phase is an ideal Weyl semimetal, which exhibits a single pair of type-I Weyl points without extra trivial Fermi pockets at the Fermi energy. In the FMc phase, the mirror M_z will protect a nodal ring on the $k_z = 0$ plane and drumheadlike surface states, as shown in Figs. 4(c) and 4(d).

E. Effective model and topological phase diagram

We build a general topological phase diagram by constructing a $k \cdot p$ model using the invariant theory [65], to more intuitively understand the role of magnetic order in the topological band structure. Since $\{C_{2y}|\tau\}$ is a key symmetry to relate two sublattices and the AFM order, three sets of Pauli matrices should be introduced to describe this system:

(i) spin σ: $|\frac{1}{2}\rangle$ and $|-\frac{1}{2}\rangle$;
(ii) orbital τ: $|\mathrm{In}\ s\rangle$ and $|\mathrm{As}\ p_z\rangle$;
(iii) sublattice ζ: $|A\rangle$ and $|B\rangle$;

and the basis are labeled by $|\Lambda_\alpha, \uparrow(\downarrow)\rangle$, where $\Lambda = \mathrm{In}, \mathrm{As}$; $\alpha = A, B$; and $\uparrow(\downarrow) = \frac{1}{2}(-\frac{1}{2})$. According to the band representation (parity $\pm$) and wavefunction at Γ, we can have the orbital basis $|\mathrm{In}_A^+\ s\rangle, |\mathrm{In}_B^+\ s\rangle, |\mathrm{As}_A^-\ p_z\rangle, |\mathrm{As}_B^-\ p_z\rangle$ [66]. The symmetry operators are given by $\hat{\mathcal{T}} = i\sigma_2\tau_0\zeta_0\mathcal{K}$, inversion $\hat{\mathcal{I}} = \sigma_0\tau_3\zeta_0$, $\hat{C}_{2z} = -i\sigma_3\tau_0\zeta_0$, and $\{\hat{C}_{2y}|\tau\} = -i\sigma_2\tau_3\zeta_1$, where $\mathcal{K}$ is the complex conjugate operator. Then we can list the irreducible representation (IR) of each matrix in Sec. SI in the Supplemental Material [59]. Based on that, the effective Hamiltonian is described by

$$\mathcal{H} = \mathcal{H}_{\mathrm{NM}} + \mathcal{H}_{ex} = \begin{pmatrix} \mathcal{H}_A & \mathcal{H}_{AB} \\ \mathcal{H}_{AB}^\dagger & \mathcal{H}_B \end{pmatrix} + \begin{pmatrix} \mathcal{H}_{\mathrm{M},A} & \mathcal{H}_{\mathrm{M},AB} \\ \mathcal{H}_{\mathrm{M},AB}^\dagger & \mathcal{H}_{\mathrm{M},B} \end{pmatrix}, \tag{4}$$

$$\begin{aligned}\mathcal{H}_{A/B} = {} & (\pm A_1 k_x + A_2 k_y)\sigma_1\tau_1 + (B_1 k_x \pm B_2 k_y)\sigma_2\tau_1 \pm C_1 k_z \sigma_3\tau_1 \\ & + D_1 k_z \sigma_0\tau_2 + E_{01}\sigma_0\tau_0 + \left(F_{01} + F_1 k_x^2 + F_2 k_y^2 + F_3 k_z^2 \pm F_4 k_x k_y\right)\sigma_0\tau_3,\end{aligned} \tag{5}$$

$$\mathcal{H}_{AB} = A_3 k_y \sigma_1 \tau_1 + B_3 k_x \sigma_2 \tau_1 + D_2 k_z \sigma_0 \tau_2 + E_{02} \sigma_0 \tau_0 + F_{02} \sigma_0 \tau_3 - iG_0 \sigma_3 \tau_0 - iL_0 \sigma_3 \tau_3 - iM_1 k_x \sigma_1 \tau_2 - iN_1 k_y \sigma_2 \tau_2 - iO_1 k_z \sigma_3 \tau_2, \quad (6)$$

where F_{01} controls the bandgap so it can be approximately treated as the inverse of the effective SOC strength. Experimentally, F_{01} is tuned by pnictide doping or pressure [67]. The other material-dependent parameters are chosen to make dispersion close to Γ qualitatively or semiquantitatively consistent with Fig. 2(b).

We next consider the exchange coupling terms $\mathcal{H}_{ex}$, namely, $\mathcal{T}$-odd terms when introducing spin orders. Note that the AFMa phase shares the same IR with FMb (also for AFMb and FMa), so both the on-site terms $\sigma_1\tau_0\zeta_3$ and $\sigma_2\tau_0\zeta_0$ will couple with IR Γ_4^+. Generally, $\mathbf{m}\cdot\boldsymbol{\sigma}$ could be taken to characterize the magnetization of one sublattice and thus to distinguish them. Take the AFMa phase as an example, we have

$$\mathcal{H}_{\mathrm{AFM}a,A/B} = \pm\,\Delta_{x1}\sigma_1\tau_0 \pm \Delta_{x2}\sigma_1\tau_3, \quad (7)$$

$$\mathcal{H}_{\mathrm{AFM}a,AB} = \Delta_3\sigma_2\tau_0 + \Delta_4\sigma_2\tau_3. \quad (8)$$

Similarly, the exchange terms for the FMa, AFMb, and AFMc phases can be obtained, respectively. Additionally, the intermediate phases between them can be expressed as a linear combination.

By numerically solving the model, we construct a $\mathcal{T}$-broken phase diagram (Fig. 5) as functions of F_{01} and α, β, γ. We find $Eu_3In_2As_4$ can be very well mapped onto the gray horizontal line with $F_{01} = 0.26$ eV. As an intermediate region between two insulating phases, the chance of being a Weyl semimetal is intimately related to the magnetic configuration. Within the FM order, the Zeeman effect results in a large semimetallic region. Then it shrinks to a fairly narrow range in the AFMa/b or tilted phase, and eventually vanishes in the AFMc phase. The axion insulator phase is quite robust against the perturbation on orientations of the AFM order in $Eu_3In_2As_4$. The model parameters and verification are provided in Sec. III in the Supplemental Material [59].

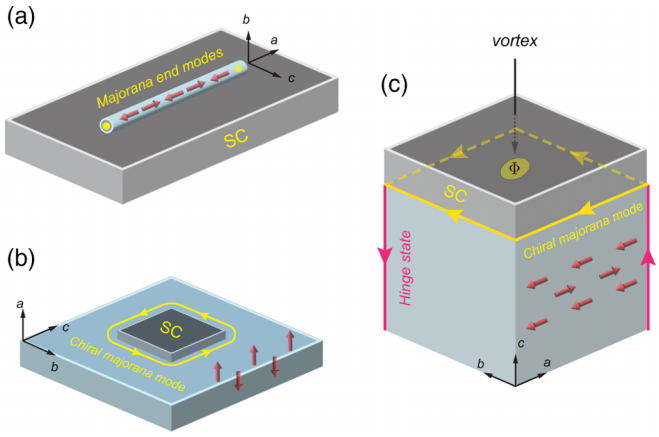

FIG. 5. Schmatics of the axion insulator $Eu_3In_2As_4$ (cyan-blue) in proximity to an s-wave superconductor (SC) (gray). (a) The nanowire configuration. (b) The SC proximity to the gapped surface, e.g., the ac/bc surfaces in AFMa phase. (c) The SC proximity to the gapless surface, e.g., the ab surface in the AFMa phase. One chiral hinge state (pink lines) splits into two chiral Majorana edge modes, providing an interferometer configuration. Yellow lines (dots) represent the chiral Majorana modes (Majorana end modes). The red arrows represent spin moments in the axion insulator.

III. DISCUSSION

A. Materials

We emphasize the results above also apply to $EuIn_2As_2$ and $Eu_5In_2Sb_6$, which are fitted in the phase diagram by only considering the anticrossing energy. To observe hinge states, $EuIn_2As_2$ is a bit special for the presence of both $C_{2z}\mathcal{T}$ and $C_{2x}\mathcal{T}$ symmetries by the "broken helix order" [44]. When the sample is in the orthorhombic geometry [Fig. 1(a)], the system presents a first-order topology with the only gapped (001) surface. In the hexagonal geometry [Fig. 1(b)], the $C_{2x}\mathcal{T}$ axis passing through the center of two hinges reverts the gap masses of neighboring facets so that the hinge current can appear along the c direction ($\hat{y}$). $Eu_5In_2Sb_6$ exhibits the same boundary states as $Eu_3In_2As_4$ because spin moments are aligned in a collinear or coplanar way to present only $C_{2z}\mathcal{T}$ [50].

The hybrid-order topology could also emerge in systems summarized in Table I, and hatches different surface-dependent quantum geometry. Besides χ^{QMD}, the second-order Hall conductivity also includes contributions from the Drude weight χ^{D} (nongeometric) and Berry curvature dipole χ^{BCD} (imaginary part of the quantum geometry) [40]. On the $C_2\mathcal{T}$-preserved surfaces, the surface quantum geometry only contains χ^{QMD}. In other systems, the surface NLAHE tensors allowed are elaborated below and in Sec. IV in the Supplemental Material [59]. First, in $\mathcal{T}$-preserved TCIs, $C_{2,4,6}$ symmetry eliminates all the surface $\chi^{ii;j}$ tensors while mirror/glide planes only permit χ^{BCD}. Second, in $\mathcal{T}$-broken TCIs, the mirror/glide symmetry accommodates both χ^{BCD}

TABLE I. Emergence of a hybrid-order topology classified from symmetries. The details are explained in Sec. IV in the Supplemental Material. Here, the mirror plane (M) must go through both the crystal surface and hinges (e.g., SnTe). The glide symmetry (G) is restricted to exist only on one set of surfaces (e.g., (100) surface of the canted AFM $MnBi_2Te_4$ [14]). When more than one following symmetries exist, the hybrid-order topology may be quenched to the first-order.

Hinge states	$\mathcal{T}$	Symmetries on the surface	Surface QAHE and surface NLAHE
Helical	✓	C_2, C_4, C_6	
		M [6], G [9]	χ^{BCD}
Chiral	×	$C_4\mathcal{T}$	$\overline{\mathbb{C}}$
		$C_2\mathcal{T}, C_6\mathcal{T}$	$\overline{\mathbb{C}}, \chi^{\mathrm{D}}, \chi^{\mathrm{QMD}}$
		M, G [14]	$\overline{\mathbb{C}}, \chi^{\mathrm{D}}, \chi^{\mathrm{BCD}}, \chi^{\mathrm{QMD}}$

and χ^{QMD}. However, it is fragile against magnetic perturbation and thus hard to protect surface/hinge states. Overall, the surface NLAHE is driven by surface states rather than hinge states.

B. Topological superconductivity

$Eu_3In_2As_4$ nanowires were recently grown from InAs nanowires by a topotaxial mutual-exchange method [51] and can inherit good interface quality to the ordinary superconductor (e.g., Al) [58]. Because of the intrinsic magnetism, strong SOC effect, and topological surface states, $Eu_3In_2As_4$ paves an appealing avenue to explore Majorana physics, as illustrated in Fig. 5. The intrinsic magnetism and SOC together lift the spin degeneracy and an odd number of Fermi surfaces can be realized at an accessible chemical potential, which is the precondition to design structure with Majorana [68,69]. (i) In a nanowire configuration [70,71], the finite size effect gaps the hinge and surface states, leading to nondegenerate topology-driven nanowire bands. In proximity to an s-wave superconductor, localized zero-energy Majorana modes will arise at two ends. Compared to earlier proposals [72,73], we do not require an external magnetic field to break time-reversal symmetry here. (ii) On the gapped surface (e.g., ac/bc facet), one can deposit a superconductor island and expect chiral Majorana edge states around the island, if the superconductor's gap Δ overcomes the magnetization-induced surface gap h. Using Fu and Kane's proposal [3,68], we expect a stable nontrivial pairing by covering a superconductor on ac or bc surfaces (criterion $|h| < \Delta$ when the Fermi energy lies inside the gap). In this case, 1D chiral Majorana modes appear at the interface between the axion insulator's surface and a superconductor region [74]. If the Fermi energy crosses an odd number of Dirac bands (metallic regime), similar chiral Majorana modes also appear in this case. (iii) On the gapless surface (e.g., ab facet in AFMa), covering a superconductor on the whole surface may lead to copropagating 1D chiral Majorana edge modes. Two Majorana modes merge into one chiral electronic state at the hinge [75]. As illustrated by Fig. 5(c), two chiral Majorana modes and two chiral hinge states naturally form a Mach-Zehnder interferometer, in which the conductance between two chiral hinge modes depends on the parity of the number of enclosed vortices in the superconductor region [74,76].

In summary, through first-principle calculations and the $k \cdot p$ model, we reveal the coexistence of the unpinned Dirac surface and chiral hinge states in $Eu_{2n+1}In_2(As,Sb)_{2n+2}$. Established by $C_2\mathcal{T}$ symmetry, such a hybrid-order topology also leads to a surface-dependent quantum geometry. Our findings on the nonlinear transport suggest new fingerprint evidence of magnetic axion insulators and other $\mathcal{T}$-preserved TCIs. Since the single crystals and nanowires of $Eu_3In_2As_4$ are readily synthesized, angle-resolved photoemission spectroscopy (ARPES), scanning tunneling spectroscopy (STS), and other techniques are called to detect these topological surface states, hinge states, and Weyl points/Fermi arcs and explore their coupling to magnetism and superconductivity.

IV. METHODS

Density-functional theory (DFT) calculations are performed with the Vienna *ab initio* simulation package (VASP) using the projector-augmented wave method [77–79]. The exchange-correlation functional based on generalized gradient approximation (GGA) parametrized by Perdew-Burke-Ernzerhof (PBE) [80] and the nonempirical strongly constrained and appropriately normed (SCAN) [81] is adopted. The kinetic energy cutoff of the plane-wave basis is set to 400 eV. The Brillouin zone integration is performed by using $8 \times 5 \times 10$ Γ-centered k point mesh. To treat the correlation effect of localized $4f$ electrons of Eu, the DFT + U method by Dudarev *et al.* is employed [82]. The details about the DFT functional choice, Hubbard U, and the Green's function [83] can be found in Sec. II in the Supplemental Material [59].

We construct the maximally localized Wannier functions of In-5s and As-4p orbitals by using WANNIER90 package [84]. The local Chern number (geometric part of the local AHC) is calculated by using a 121×121 k mesh [32]. The nonlinear surface Hall conductivity is performed on the $k \cdot p$ Hamiltonian using an 800×800 k mesh. The complete formula of the second-order nonlinear conductivity reads as

$$\begin{aligned}\sigma_{ij;k} &= \chi^{\mathrm{D}}_{ij;k} + \chi^{\mathrm{BCD}}_{ij;k} + \chi^{\mathrm{QMD}}_{ij;k} \\ &= -\frac{e^3\tau^2}{\hbar^3}\sum_n \int_{\boldsymbol{k}} f_n \partial_{k_i}\partial_{k_j}\partial_{k_k}\varepsilon_n \\ &\quad - \frac{e^3\tau}{\hbar^2}\sum_n \int_{\boldsymbol{k}} f_n\left(\partial_{k_i}\Omega_n^{jk} + \partial_{k_j}\Omega_n^{ik}\right) \\ &\quad - \frac{e^3}{\hbar}\sum_n \int_{\boldsymbol{k}} f_n\left(2\partial_{k_k}\mathcal{G}^{ij}_{\boldsymbol{k}} - \frac{1}{2}\left(\partial_{k_i}\mathcal{G}_n^{jk} + \partial_{k_j}\mathcal{G}_n^{ik}\right)\right), \quad (9)\end{aligned}$$

where $\Omega_n = \sum_{m\neq n}\Omega_{nm}$ is the Berry curvature, and $\mathcal{G}_n = \sum_{m\neq n} 2g_{nm}/(\varepsilon_n - \varepsilon_m)$ is the band-normalized quantum metric.

Note added. After we posted the manuscript, an experimental work was posted to report a pair of Weyl nodes in the ferromagnetic phase under an external magnetic field [52], consistent with our theory.

ACKNOWLEDGMENTS

We are inspired by a recent experimental work by Haim Beidenkopf and Hadas Shtrikman. We thank Xi Dai, Mingqiang Gu, Hengxin Tan, and Zhiqiang Mao for helpful discussions. C.X.L. acknowledges the support of NSF Grant No. DMR-2241327. B.Y. acknowledges the financial support by the European Research Council (ERC Consolidator Grant "NonlinearTopo," No. 815869) and the ISF - Personal Research Grant (No. 2932/21).

[1] M. Z. Hasan and C. L. Kane, Colloquium: Topological insulators, Rev. Mod. Phys. **82**, 3045 (2010).

[2] X.-L. Qi and S.-C. Zhang, Topological insulators and superconductors, Rev. Mod. Phys. **83**, 1057 (2011).

[3] Y. Tokura, K. Yasuda, and A. Tsukazaki, Magnetic topological insulators, Nat. Rev. Phys. **1**, 126 (2019).

[4] Y. L. Chen, J. G. Analytis, J.-H. Chu, Z. K. Liu, S.-K. Mo, X.-L. Qi, H. J. Zhang, D. H. Lu, X. Dai, Z. Fang *et al.*, Experimental realization of a three-dimensional topological insulator, Bi_2Te_3, Science **325**, 178 (2009).

[5] H. Zhang, C.-X. Liu, X.-L. Qi, X. Dai, Z. Fang, and S.-C. Zhang, Topological insulators in Bi_2Se_3, Bi_2Te_3 and Sb_2Te_3 with a single dirac cone on the surface, Nat. Phys. **5**, 438 (2009).

[6] T. H. Hsieh, H. Lin, J. Liu, W. Duan, A. Bansil, and L. Fu, Topological crystalline insulators in the SnTe material class, Nat. Commun. **3**, 982 (2012).

[7] F. Schindler, Z. Wang, M. G. Vergniory, A. M. Cook, A. Murani, S. Sengupta, A. Y. Kasumov, R. Deblock, S. Jeon, I. Drozdov *et al.*, Higher-order topology in bismuth, Nat. Phys. **14**, 918 (2018).

[8] C. Yue, Y. Xu, Z. Song, H. Weng, Y.-M. Lu, C. Fang, and X. Dai, Symmetry-enforced chiral hinge states and surface quantum anomalous Hall effect in the magnetic axion insulator $Bi_{2-x}Sm_xSe_3$, Nat. Phys. **15**, 577 (2019).

[9] J. Ma, C. Yi, B. Lv, Z. Wang, S. Nie, L. Wang, L. Kong, Y. Huang, P. Richard, P. Zhang, K. Yaji, K. Kuroda, S. Shin, H. Weng, B. A. Bernevig, Y. Shi, T. Qian, and H. Ding, Experimental evidence of hourglass fermion in the candidate nonsymmorphic topological insulator KHgSb, Sci. Adv. **3**, e1602415 (2017).

[10] W. A. Benalcazar, B. A. Bernevig, and T. L. Hughes, Quantized electric multipole insulators, Science **357**, 61 (2017).

[11] Z. Song, Z. Fang, and C. Fang, (d-2)-Dimensional edge states of rotation symmetry protected topological states, Phys. Rev. Lett. **119**, 246402 (2017).

[12] Z. Wang, B. J. Wieder, J. Li, B. Yan, and B. A. Bernevig, Higher-order topology, monopole nodal lines, and the origin of large fermi arcs in transition metal dichalcogenides XTe_2 (X = Mo, W), Phys. Rev. Lett. **123**, 186401 (2019).

[13] C.-Z. Chang, J. Zhang, X. Feng, J. Shen, Z. Zhang, M. Guo, K. Li, Y. Ou, P. Wei, L.-L. Wang *et al.*, Experimental observation of the quantum anomalous Hall effect in a magnetic topological insulator, Science **340**, 167 (2013).

[14] R.-X. Zhang, F. Wu, and S. D. Sarma, Möbius insulator and higher-order topology in $MnBi_{2n}Te_{3n+1}$, Phys. Rev. Lett. **124**, 136407 (2020).

[15] Y. Xu, Z. Song, Z. Wang, H. Weng, and X. Dai, Higher-order topology of the axion insulator $EuIn_2As_2$, Phys. Rev. Lett. **122**, 256402 (2019).

[16] K. Yasuda, M. Mogi, R. Yoshimi, A. Tsukazaki, K. S. Takahashi, M. Kawasaki, F. Kagawa, and Y. Tokura, Quantized chiral edge conduction on domain walls of a magnetic topological insulator, Science **358**, 1311 (2017).

[17] P. Wadley, B. Howells, J. Železný, C. Andrews, V. Hills, R. P. Campion, V. Novák, K. Olejník, F. Maccherozzi, S. Dhesi *et al.*, Electrical switching of an antiferromagnet, Science **351**, 587 (2016).

[18] A. M. Turner, Y. Zhang, R. S. K. Mong, and A. Vishwanath, Quantized response and topology of magnetic insulators with inversion symmetry, Phys. Rev. B **85**, 165120 (2012).

[19] C. Fang and L. Fu, New classes of three-dimensional topological crystalline insulators: Nonsymmorphic and magnetic, Phys. Rev. B **91**, 161105(R) (2015).

[20] J. Ahn, D. Kim, Y. Kim, and B.-J. Yang, Band topology and linking structure of nodal line semimetals with Z_2 monopole charges, Phys. Rev. Lett. **121**, 106403 (2018).

[21] J. Ahn and B.-J. Yang, Symmetry representation approach to topological invariants in $C_{2z}T$-symmetric systems, Phys. Rev. B **99**, 235125 (2019).

[22] R. González-Hernández, C. Pinilla, and B. Uribe, Axion insulators protected by $C_2\mathbb{T}$ symmetry, their K-theory invariants, and material realizations, Phys. Rev. B **106**, 195144 (2022).

[23] R. S. K. Mong, A. M. Essin, and J. E. Moore, Antiferromagnetic topological insulators, Phys. Rev. B **81**, 245209 (2010).

[24] D. Zhang, M. Shi, T. Zhu, D. Xing, H. Zhang, and J. Wang, Topological axion states in the magnetic insulator $MnBi_2Te_4$ with the quantized magnetoelectric effect, Phys. Rev. Lett. **122**, 206401 (2019).

[25] J. Li, Y. Li, S. Du, Z. Wang, B.-L. Gu, S.-C. Zhang, K. He, W. Duan, and Y. Xu, Intrinsic magnetic topological insulators in van der Waals layered $MnBi_2Te_4$-family materials, Sci. Adv. **5**, eaaw5685 (2019).

[26] X.-L. Qi, T. L. Hughes, and S.-C. Zhang, Topological field theory of time-reversal invariant insulators, Phys. Rev. B **78**, 195424 (2008).

[27] A. M. Essin, J. E. Moore, and D. Vanderbilt, Magnetoelectric polarizability and axion electrodynamics in crystalline insulators, Phys. Rev. Lett. **102**, 146805 (2009).

[28] N. P. Armitage and L. Wu, On the matter of topological insulators as magnetoelectrics, SciPost Physics **6**, 046 (2019).

[29] C. Fang, M. J. Gilbert, and B. A. Bernevig, Bulk topological invariants in noninteracting point group symmetric insulators, Phys. Rev. B **86**, 115112 (2012).

[30] A. Sekine and K. Nomura, Axion electrodynamics in topological materials, J. Appl. Phys. **129**, 141101 (2021).

[31] C. Liu, Y. Wang, H. Li, Y. Wu, Y. Li, J. Li, K. He, Y. Xu, J. Zhang, and Y. Wang, Robust axion insulator and chern insulator phases in a two-dimensional antiferromagnetic topological insulator, Nat. Mater. **19**, 522 (2020).

[32] N. Varnava and D. Vanderbilt, Surfaces of axion insulators, Phys. Rev. B **98**, 245117 (2018).

[33] J. Provost and G. Vallee, Riemannian structure on manifolds of quantum states, Commun. Math. Phys. **76**, 289 (1980).

[34] D. Xiao, M.-C. Chang, and Q. Niu, Berry phase effects on electronic properties, Rev. Mod. Phys. **82**, 1959 (2010).

[35] M. Gu, J. Li, H. Sun, Y. Zhao, C. Liu, J. Liu, H. Lu, and Q. Liu, Spectral signatures of the surface anomalous Hall effect in magnetic axion insulators, Nat. Commun. **12**, 3524 (2021).

[36] C. Wang, Y. Gao, and D. Xiao, Intrinsic nonlinear Hall effect in antiferromagnetic tetragonal CuMnAs, Phys. Rev. Lett. **127**, 277201 (2021).

[37] H. Liu, J. Zhao, Y.-X. Huang, W. Wu, X.-L. Sheng, C. Xiao, and S. A. Yang, Intrinsic second-order anomalous Hall effect and its application in compensated antiferromagnets, Phys. Rev. Lett. **127**, 277202 (2021).

[38] N. Wang, D. Kaplan, Z. Zhang, T. Holder, N. Cao, A. Wang, X. Zhou, F. Zhou, Z. Jiang, C. Zhang *et al.*, Quantum-metric-induced nonlinear transport in a topological antiferromagnet, Nature (London) **621**, 487 (2023).

[39] A. Gao, Y.-F. Liu, J.-X. Qiu, B. Ghosh, T. V. Trevisan, Y. Onishi, C. Hu, T. Qian, H.-J. Tien, S.-W. Chen *et al.*, Quantum metric nonlinear Hall effect in a topological antiferromagnetic heterostructure, Science **381**, 181 (2023).

[40] D. Kaplan, T. Holder, and B. Yan, Unification of nonlinear anomalous Hall effect and nonreciprocal magnetoresistance in metals by the quantum geometry, Phys. Rev. Lett. **132**, 026301 (2024).

[41] A. B. Childs, S. Baranets, and S. Bobev, Five new ternary indium-arsenides discovered. Synthesis and structural characterization of the Zintl phases $Sr_3In_2As_4$, $Ba_3In_2As_4$, $Eu_3In_2As_4$, Sr_5In_2As6 and $Eu_5In_2As_6$, J. Solid State Chem. **278**, 120889 (2019).

[42] Y. Zhang, K. Deng, X. Zhang, M. Wang, Y. Wang, C. Liu, J.-W. Mei, S. Kumar, E. F. Schwier, K. Shimada, C. Chen, and B. Shen, In-plane antiferromagnetic moments and magnetic polaron in the axion topological insulator candidate $EuIn_2As_2$, Phys. Rev. B **101**, 205126 (2020).

[43] T. Sato, Z. Wang, D. Takane, S. Souma, C. Cui, Y. Li, K. Nakayama, T. Kawakami, Y. Kubota, C. Cacho, T. K. Kim, A. Arab, V. N. Strocov, Y. Yao, and T. Takahashi, Signature of band inversion in the antiferromagnetic phase of axion insulator candidate $EuIn_2As_2$, Phys. Rev. Res. **2**, 033342 (2020).

[44] S. X. Riberolles, T. V. Trevisan, B. Kuthanazhi, T. Heitmann, F. Ye, D. Johnston, S. Bud'ko, D. Ryan, P. Canfield, A. Kreyssig *et al.*, Magnetic crystalline-symmetry-protected axion electrodynamics and field-tunable unpinned Dirac cones in $EuIn_2As_2$, Nat. Commun. **12**, 999 (2021).

[45] J.-R. Soh, A. Bombardi, F. Mila, M. C. Rahn, D. Prabhakaran, S. Francoual, H. M. Rønnow, and A. T. Boothroyd, Understanding unconventional magnetic order in a candidate axion insulator by resonant elastic x-ray scattering, Nat. Commun. **14**, 3387 (2023).

[46] E. Donoway, T. V. Trevisan, A. L. Peláez, R. P. Day, K. Yamakawa, Y. Sun, J. R. Soh, D. Prabhakaran, A. T. Boothroyd, R. M. Fernandes, J. G. Analytis, J. E. Moore, J. Orenstein, and V. Sunko, Symmetry-breaking pathway towards the unpinned broken helix, arXiv:2310.16018 [cond-mat.str-el].

[47] P. Rosa, Y. Xu, M. Rahn, J. Souza, S. Kushwaha, L. Veiga, A. Bombardi, S. Thomas, M. Janoschek, E. Bauer *et al.*, Colossal magnetoresistance in a nonsymmorphic antiferromagnetic insulator, npj Quantum Mater. **5**, 52 (2020).

[48] M. V. Crivillero, S. Rößler, P. F. S. Rosa, J. Müller, U. K. Rößler, and S. Wirth, Surface and electronic structure at atomic length scales of the nonsymmorphic antiferromagnet $Eu_5In_2Sb_6$, Phys. Rev. B **106**, 035124 (2022).

[49] M. C. Rahn, M. N. Wilson, T. J. Hicken, F. L. Pratt, C. Wang, F. Orlandi, D. D. Khalyavin, P. Manuel, L. S. I. Veiga, A. Bombardi, S. Francoual, P. Bereciartua, A. S. Sukhanov, J. D. Thompson, S. M. Thomas, P. F. S. Rosa, T. Lancaster, F. Ronning, and M. Janoschek, Magnetism in the axion insulator candidate $Eu_5In_2Sb_6$, Phys. Rev. B **109**, 174404 (2024).

[50] V. C. Morano, J. Gaudet, N. Varnava, T. Berry, T. Halloran, C. J. Lygouras, X. Wang, C. M. Hoffman, G. Xu, J. W. Lynn, T. M. McQueen, D. Vanderbilt, and C. L. Broholm, Noncollinear 2k antiferromagnetism in the Zintl semiconductor $Eu_5In_2Sb_6$, Phys. Rev. B **109**, 014432 (2024).

[51] M. S. Song, L. Houben, Y. Zhao, H. Bae, N. Rothem, A. Gupta, B. Yan, B. Kalisky, M. Zaluska-Kotur, P. Kacman *et al.*, Topotaxial mutual-exchange growth of magnetic Zintl $Eu_3In_2As_4$ nanowires with axion insulator classification, Nat. Nanotechnol. 1 (2024).

[52] K. Jia, J. Yao, X. He, Y. Li, J. Deng, M. Yang, J. Wang, Z. Zhu, C. Wang, D. Yan, H. L. Feng, J. Shen, Y. Luo, Z. Wang, and Y. Shi, Discovery of a magnetic topological semimetal $Eu_3In_2As_4$ with a single pair of Weyl points, arXiv:2403.07637 [cond-mat.mes-hall].

[53] P. Liu, J. Li, J. Han, X. Wan, and Q. Liu, Spin-group symmetry in magnetic materials with negligible spin-orbit coupling, Phys. Rev. X **12**, 021016 (2022).

[54] L. Šmejkal, J. Sinova, and T. Jungwirth, Beyond conventional ferromagnetism and antiferromagnetism: A phase with nonrelativistic spin and crystal rotation symmetry, Phys. Rev. X **12**, 031042 (2022).

[55] L. Šmejkal, J. Sinova, and T. Jungwirth, Emerging research landscape of altermagnetism, Phys. Rev. X **12**, 040501 (2022).

[56] J. Krempask, L. Šmejkal, S. D'Souza, M. Hajlaoui, G. Springholz, K. Uhlířová, F. Alarab, P. Constantinou, V. Strocov, D. Usanov *et al.*, Altermagnetic lifting of kramers spin degeneracy, Nature (London) **626**, 517 (2024).

[57] Y.-P. Zhu, X. Chen, X.-R. Liu, Y. Liu, P. Liu, H. Zha, G. Qu, C. Hong, J. Li, Z. Jiang *et al.*, Observation of plaid-like spin splitting in a noncoplanar antiferromagnet, Nature (London) **626**, 523 (2024).

[58] A. Das, Y. Ronen, Y. Most, Y. Oreg, M. Heiblum, and H. Shtrikman, Zero-bias peaks and splitting in an Al–InAs nanowire topological superconductor as a signature of Majorana fermions, Nat. Phys. **8**, 887 (2012).

[59] See Supplemental Material at http://link.aps.org/supplemental/10.1103/PhysRevB.110.205111 for additional electronic structure and parameter details.

[60] O. Pozo, C. Repellin, and A. G. Grushin, Quantization in chiral higher order topological insulators: Circular dichroism and local Chern marker, Phys. Rev. Lett. **123**, 247401 (2019).

[61] M. Pan, D. Li, J. Fan, and H. Huang, Two-dimensional Stiefel-Whitney insulators in liganded xenes, npj Comput. Mater. **8**, 1 (2022).

[62] Z. Guo, J. Deng, Y. Xie, and Z. Wang, Quadrupole topological insulators in $Ta_3M_3Te_5$ (M = Ni, Pd) monolayers, npj Quantum Mater. **7**, 87 (2022).

[63] T. Rauch, T. Olsen, D. Vanderbilt, and I. Souza, Geometric and nongeometric contributions to the surface anomalous Hall conductivity, Phys. Rev. B **98**, 115108 (2018).

[64] R. Chen, S. Li, H.-P. Sun, Q. Liu, Y. Zhao, H.-Z. Lu, and X. C. Xie, Using nonlocal surface transport to identify the axion insulator, Phys. Rev. B **103**, L241409 (2021).

[65] C.-X. Liu, X.-L. Qi, H. J. Zhang, X. Dai, Z. Fang, and S.-C. Zhang, Model Hamiltonian for topological insulators, Phys. Rev. B **82**, 045122 (2010).

[66] M. N. Rasul, M. Mehmood, T. Hu, A. Hussain, M. A. Rafiq, and F. Iqbal, First principles calculations of the properties of $Sr_3In_2As_4$ and $Eu_3In_2As_4$ Zintl phases, J. Mater. Sci. **58**, 16753 (2023).

[67] N. Varnava, T. Berry, T. M. McQueen, and D. Vanderbilt, Engineering magnetic topological insulators in $Eu_5M_2X_6$ Zintl compounds, Phys. Rev. B **105**, 235128 (2022).

[68] L. Fu and C. L. Kane, Superconducting proximity effect and Majorana fermions at the surface of a topological insulator, Phys. Rev. Lett. **100**, 096407 (2008).

[69] S. A. A. Ghorashi, T. L. Hughes, and J. Cano, Altermagnetic routes to Majorana modes in zero net magnetization, arXiv:2306.09413 [cond-mat.mes-hall].

[70] R. M. Lutchyn, J. D. Sau, and S. Das Sarma, Majorana fermions and a topological phase transition in semiconductor-superconductor heterostructures, Phys. Rev. Lett. **105**, 077001 (2010).

[71] Y. Oreg, G. Refael, and F. von Oppen, Helical liquids and Majorana bound states in quantum wires, Phys. Rev. Lett. **105**, 177002 (2010).

[72] A. Cook and M. Franz, Majorana fermions in a topological-insulator nanowire proximity-coupled to an *s*-wave superconductor, Phys. Rev. B **84**, 201105(R) (2011).

[73] J. Alicea, New directions in the pursuit of Majorana fermions in solid state systems, Rep. Prog. Phys. **75**, 076501 (2012).

[74] A. R. Akhmerov, J. Nilsson, and C. W. J. Beenakker, Electrically detected interferometry of Majorana fermions in a topological insulator, Phys. Rev. Lett. **102**, 216404 (2009).

[75] J. Wang, Q. Zhou, B. Lian, and S.-C. Zhang, Chiral topological superconductor and half-integer conductance plateau from quantum anomalous Hall plateau transition, Phys. Rev. B **92**, 064520 (2015).

[76] L. Fu and C. L. Kane, Probing neutral Majorana fermion edge modes with charge transport, Phys. Rev. Lett. **102**, 216403 (2009).

[77] G. Kresse and J. Furthmüller, Efficient iterative schemes for *ab initio* total-energy calculations using a plane-wave basis set, Phys. Rev. B **54**, 11169 (1996).

[78] G. Kresse and D. Joubert, From ultrasoft pseudopotentials to the projector augmented-wave method, Phys. Rev. B **59**, 1758 (1999).

[79] P. E. Blöchl, Projector augmented-wave method, Phys. Rev. B **50**, 17953 (1994).

[80] J. P. Perdew, K. Burke, and M. Ernzerhof, Generalized gradient approximation made simple, Phys. Rev. Lett. **77**, 3865 (1996).

[81] J. Sun, A. Ruzsinszky, and J. P. Perdew, Strongly constrained and appropriately normed semilocal density functional, Phys. Rev. Lett. **115**, 036402 (2015).

[82] S. L. Dudarev, G. A. Botton, S. Y. Savrasov, C. J. Humphreys, and A. P. Sutton, Electron-energy-loss spectra and the structural stability of nickel oxide: An LSDA+U study, Phys. Rev. B **57**, 1505 (1998).

[83] M. P. Lopez Sancho, J. M. Lopez Sancho, J. M. L. Sancho, and J. Rubio, Highly convergent schemes for the calculation of bulk and surface green functions, J. Phys. F **15**, 851 (1985).

[84] I. Souza, N. Marzari, and D. Vanderbilt, Maximally localized Wannier functions for entangled energy bands, Phys. Rev. B **65**, 035109 (2001).